



# In situ engineering bi-metallic phospho-nitride bi-functional electrocatalysts for overall water splitting

Rui Zhang<sup>a,1</sup>, Jun Huang<sup>b,1</sup>, Guangliang Chen<sup>a,\*</sup>, Wei Chen<sup>b,\*</sup>, Changsheng Song<sup>a,\*</sup>, Chaorong Li<sup>a</sup>, Kostya Ostrikov (Ken)<sup>c</sup>

<sup>a</sup> Key Laboratory of Advanced Textile Materials and Manufacturing Technology and Engineering Research Center for Eco-Dyeing & Finishing of Textiles, Ministry of Education, Zhejiang Sci-Tech University, Hangzhou, 310018, China

<sup>b</sup> College of Physics and Electronic Information, Gannan Normal University, Ganzhou, Jiangxi, 341000, China

<sup>c</sup> School of Chemistry, Physics and Mechanical Engineering, Queensland University of Technology, Brisbane, QLD, 4000, Australia

## ARTICLE INFO

### Keywords:

Metal phosphide  
Electrocatalysis  
Overall water splitting  
N-doping  
Plasma processing

## ABSTRACT

In situ engineering highly active and ultrastable bi-functional electrocatalysts based on metal ions from transition metal alloys that are simultaneously suitable for hydrogen evolution reaction (HER) and oxygen evolution reaction (OER) is one of the key unresolved challenges on the way to energy-efficient hydrogen fuel production by water splitting. One such novel catalyst based on polyhedron N-doped Ni-Co phosphide is burgeoned directly from the Ni-Co foam (N-NiCoP/NCF) using a facile and eco-friendly approach without involving heavy metal ions. The N-NiCoP/NCF catalyst exhibits superior activity in 1.0 M KOH for overall water splitting, evidenced by the low overpotentials of 78 mV for HER and 225 mV for OER at a current density of 10 mA cm<sup>-2</sup>. The excellent electrocatalytic activity of N-NiCoP is attributed to the increased Fermi level due to effective N-doping and the abundant exposed active crystal planes (311) of heterostructured Co<sub>2</sub>NiP<sub>4</sub> phase. Importantly, the N-NiCoP/NCF catalyst shows ultra-stable electrocatalytic performance while retaining structural integrity in both HER and OER processes during continuous reactions for over 100 h. These results open new avenues for in situ engineering of transition-metal based electrocatalysts used for renewable energy generation.

## 1. Introduction

Electrocatalytic water splitting is one of the most promising processes for virtually inexhaustible and carbon emissions-free hydrogen fuel generation [1,2]. The process involves two separate reactions for hydrogen evolution reaction (HER) on a cathode and oxygen evolution reaction (OER) on the anode, usually both requiring different catalysts [3–8]. Despite decades of research it remains challenging to develop a universal (bi-functional) catalyst for the both reactions and reduce the energy costs (lower the over-potentials needed to achieve the benchmark current of at 10 mA cm<sup>-2</sup> in industrial electrolyzers) and achieve stable catalyst performance under industry-relevant conditions [9–11]. Solution of this challenge is expected to be a radical breakthrough in the electrocatalysis and relevant energy materials and electrochemistry fields and is poised to help hydrogen economy become a common reality in the coming years.

In recent years, compared with other transition metal derivatives (e.g., sulfides [12–14], nitrides [15,16], and selenides [17–19]),

electrocatalysts based on transition metal phosphide (TMP) have emerged as highly-promising candidates for overall water splitting, with enormous potential for broader applications in the green and sustainable energy fields [20–25]. However, their performance as bi-functional electrocatalysts has been severely hampered owing to several major fundamental limitations in the ability to (i) control their conductivity and electron bands by hetero-atom doping (e.g., N-doping for HER and P-doping for OER) [8,26,27], (ii) create highly-catalytically reactive crystal facets, and (iii) produce micro- and nanocrystalline features without additional deposition steps of one or more metals, ultimately leading to unsatisfactory operation stability under harsh real-world (e.g., strongly basic, pH 14) conditions.

These problems are particularly severe for one of the most promising NiCo systems, where it is extremely difficult to (i) evolve stable NiCo nanoscale features without additional metal deposition and (ii) achieve simultaneous incorporation of N and P atoms in sufficient amounts to be effective in the both HER and OER processes, importantly (iii) while retaining or even improving the stability of operation. Furthermore, we

\* Corresponding authors.

E-mail addresses: [glchen@zstu.edu.cn](mailto:glchen@zstu.edu.cn) (G. Chen), [chwbetter@163.com](mailto:chwbetter@163.com) (W. Chen), [cssong@zstu.edu.cn](mailto:cssong@zstu.edu.cn) (C. Song).

<sup>1</sup> These authors contributed equally to this work.

are not aware of successful attempts of effective control of the reactive facets of NiCo phosphides (NCPs), specifically targeting the HER and OER performances.

Here, we develop and demonstrate our innovative solution stemming from a new concept based on conversion of a rigid NiCo alloy foam into a hydroxide form, followed by the effective, simultaneous doping by N and P using highly-reactive  $N_2/PH_3$  plasmas. This solution not only allowed us to control the reactive planes (e.g., dominant (311) facets), the effective N and P dopant incorporation, but also to dramatically increase the catalyst activity and stability under industry-relevant conditions. We further use numerical simulations to discover the mechanisms of effective control of the Fermi level and electron conductivity leading to the outstanding overall catalyst performance including the energy efficiency and long-term stability. More importantly, we demonstrate that the catalyst structure retains integrity undergoing a harsh HER or OER process for 100 h. This innovative combination of the approaches has never been successfully used for the NCPs energy materials systems and is promising well beyond the water electrolysis field.

## 2. Experimental section

### 2.1. Chemicals and reagents

Ni-Co foam (NCF) (thickness: 0.5 mm) was obtained from Kunshan Jiayisheng Electronics Co., Ltd. Ethyl alcohol ( $CH_3CH_2OH$ , 99.7%), acetone ( $CH_3COCH_3$ ,  $\geq 99.5\%$ ), sodium hydroxide (NaOH, 96.0%), ammonium persulfate ( $(NH_4)_2S_2O_8$ , 98.0%), sodium hypophosphite ( $NaH_2PO_2$ , 99.0%), potassium hydroxide (KOH,  $\geq 85.0\%$ ), Pt/C (20 wt %), and ruthenium oxide ( $RuO_2$ , 99.9%) were purchased from the Hangzhou Mike Chemical Instrument Co., Ltd. All chemicals were of analytical grade, and used without further purification. Deionized water was used in all experiments.

### 2.2. Materials preparation

#### 2.2.1. In situ synthesis of $NiCo(OH)_x/NCF$

Firstly, the NCF ( $1.5 \times 2.5$  cm) was carefully cleaned with acetone (15 mL), ethanol and water in an ultrasound bath, respectively. Then, the cleaned NCF was dried in an oven at  $50^\circ C$  for 4 h. The  $NiCo(OH)_x/NCF$  was prepared with a hydrothermal based method, and the detail processes were performed as followed: (1) The 2.5 M of sodium hydroxide and 0.125 M ammonium persulfate were dissolved into 20 mL deionized water, magnetically stirring to form a transparent solution; (2) After that, the solution and the NCF were transferred to a 30 mL Teflon-lined stainless-steel autoclave, and the autoclave was maintained at  $180^\circ C$  for 18 h in an electric oven. After that, the bulk crystal structure of NiCo hydroxide on NCF precursor was taken out, and washed with deionized water for three times. Lastly, the  $NiCo(OH)_x/NCF$  was oven-dried at  $50^\circ C$  for 2 h. For a comparison, the samples with different reactive temperature and reagent concentration were also prepared using a similar process. In order to navigate among the different samples used in our work, we have summarized the nomenclature of different samples, as shown in Table S1.

#### 2.2.2. Synthesis of $N-NiCoP/NCF$

The  $NiCo(OH)_x/NCF$  samples fabricated with the optimized parameters were placed in a plasma enhanced chemical vapor deposition (PECVD) system, where the temperature was maintained at  $250^\circ C$ . The two ring-shaped electrodes encircling the quartz tube were connected to a commercial radio-frequency source (Changzhou Rishige Co. Ltd., 13.56 MHz). The  $NaH_2PO_4$  (1 g) contained in a stainless device was heated at  $300^\circ C$  to produce the  $PH_3$  gas, and the argon (Ar) and nitrogen ( $N_2$ ) gases (ratio: 50/50 sccm) carried the  $PH_3$  monomer to the PECVD system, where the reactive pressure was 50 Pa. Under the operation of Ar/ $N_2$  plasma (60 W) with  $PH_3$  monomer for 2 h, the  $NiCo(OH)_x/NCF$  was transformed to the  $N-NiCoP/NCF$ , and the mass loading

on the NCF surface was about  $\sim 2.085 \text{ mg cm}^{-2}$ . In addition, the effect of reactive gases (Ar: 100 sccm;  $N_2$ : 100 sccm) on the physicochemical structure of  $NiCoP/NCF$  catalyst was also investigated. For comparison, the  $NiCoP/NCF$  was also treated with similar reactive conditions in the PECVD device without generating plasmas. Meanwhile, the  $NiCoP$  was also prepared by treating the NCF substrate with the  $N_2-PH_3$  plasma at  $250^\circ C$ .

### 2.3. Materials characterization

The morphology of the samples was characterized by using a JSM-6700F field-emission scanning electron microscopy (FE-SEM, JEOL, Japan) and transmission electron microscopy (TEM, Model JSM-2100, JEOL, Japan). The crystalline phases of  $N-NiCoP/NCF$  were analyzed with an X-ray diffractometer (XRD, Thermo Fisher Scientific, USA) using a Cu  $K\alpha$  radiation source at 35 kV. X-ray photoelectron spectroscopy (XPS, K-Alpha, USA) with the X-ray source operating at 300 W (Al  $K\alpha$ : 1486.6 eV) was utilized to examine the surface chemical composition of as-prepared samples. It should be noted that the high resolution peaks of the elements were deconvoluted using XPSPEAK41 software, and the base line was linear or Shirley modle according to the peak profiles. The frame structures of the materials were detected by a Raman spectroscope (Model: Lab Ram HRUV) equipped with a DPSS laser source with the 532 nm wavelength, and the amount of  $N-NiCoP/NCF$  was determined by a precision microbalance (delta: 0.001 mg).

### 2.4. Electrochemical measurements

All of the HER and OER electrochemical tests were performed in a standard three-electrode system on an electrochemical workstation (Model CHI660E, Shanghai Chenhua Instrument Co., Ltd.). A carbon rod was employed as a counter electrode, and the Hg/HgO acted as the reference electrodes for measuring HER and OER activity of the catalyst, respectively. All the tests were carried out in 1 M KOH [28]. The loaded NCF were tailored into  $0.5 \text{ cm} \times 0.5 \text{ cm}$  samples and directly acted as the working electrodes for the electrochemical tests. The cyclic voltammetry (CV), linear sweep voltammetry (LSV), electrochemical impedance spectroscopy (EIS) and chronoamperometry tests were performed. The working electrodes were activated by using a CV test at a scan rate of  $50 \text{ mV s}^{-1}$  for 800 sweep segments. LSV was conducted at a scan rate of  $1 \text{ mV s}^{-1}$ , and the HER and OER performances can be analyzed by the obtained LSV and Tafel curves. All the potentials were calibrated with respect to the reversible hydrogen electrode (RHE) according to Nernst equation in 1 M KOH as follows:  $E \text{ vs RHE} = E \text{ vs Hg/HgO} + 0.095 + 0.059 \text{ pH}$  [29], and all of the potentials in the LSV polarization curves were iR-corrected with respect to the ohmic resistance of the solution. EIS were recorded in the frequency range from 100 kHz to 0.1 Hz with 10 points per decade by using an AC voltage with the 5 mV amplitude. For long-term CV cycling tests of HER and OER reactions, the  $N-NiCoP/NCF$  electrodes were tested at a scan rate of  $100 \text{ mV s}^{-1}$  for 10,000 cycles first, and the final CV polarization curves were recorded at a scan rate of  $1 \text{ mV s}^{-1}$  again. The stability of the catalyst electrodes were assessed by chronoamperometry with a constant current of  $10 \text{ mA cm}^{-2}$ . The mass loading on the NCF surface was about  $\sim 2.085 \text{ mg cm}^{-2}$  for the  $N-NiCoP/NCF$  electrode. As a comparison, the NCF coated with 20 wt % Pt/C and  $RuO_2$  at the same mass loading rate ( $2.085 \text{ mg/cm}^2$ ) act as the negative electrode and the anode, respectively. Meanwhile, the approaches used for analyzing electrocatalytic activity of Pt/C, calculating the electrochemical double layer capacitances ( $C_{dl}$ ) and turn over frequencies (TOF) followed the established protocols as reported previously [28,30]. The amounts of evolved  $H_2$  and  $O_2$  gases were measured by a water drainage approach in a vacuum-grade reactor. The reactor had two separate reaction chambers that were connected by a narrow gap (0.5 cm) to allow the alkaline electrolyte to be the same in both chambers. Two electrodes, one sample-supporting electrode and the other a counter-electrode

(carbon rod), were respectively fitted into the two chambers. The number of moles of the collected gases that were generated from the reactions was calculated using the ideal gas approximation.

## 2.5. DFT calculations

Theoretical calculations have been performed within the framework of density functional theory (DFT) by the Vienna an initio Simulation Package (VASP) as implemented in our former work [31]. The exchange-correlation energy was treated in the generalized-gradient (GGA) using Perdew-Burke-Ernzerhof PBE method [32]. The N-NiCoP model was approximate constructed on the  $5 \times 5$  supercell with 4 N doped in  $\text{Ni}_4\text{Co}_{21}\text{P}_{21}$ . The cutoff energy of plane wave was chosen at 300 eV. For the structure optimizations,  $6 \times 6 \times 6$  Monkhorst-Pack (MP) grids were used. The changes in total energies between two successive iteration steps were less than  $10^{-5}$  eV, and all the Hellmann-Feynman force acting on each atoms was lower than 0.001 eV/Å.

## 3. Results and discussion

### 3.1. Fabrication and characterization

The whole fabrication process for N-NiCoP/NCF is summarized in Fig. 1a. The commercial Ni-Co foam not only acted as a substrate material, but also served as a precursor for providing transition metal elements, which make full use of the three-dimensional skeleton structure and good electron transport ability of NCF. The in situ formed bulk crystal structure of NiCo hydroxide on NCF ( $\text{NiCo}(\text{OH})_x/\text{NCF}$ ) is treated with the  $\text{N}_2/\text{Ar}-\text{PH}_3$  plasma to achieve simultaneous N-doping and phosphating. The photographs of the plasma discharges sustained in different gases are shown in Fig. 1b. Normally, the intermediate NiCo ( $\text{OH}$ )<sub>2</sub> structure keeps tight relationship with the latter fabricated NiCo phosphides. Therefore, the effect of the growth parameters for NiCo ( $\text{OH}$ )<sub>2</sub> on the HER and OER performances of N-NiCoP was firstly investigated. As shown in Figs. S1, S2 and S3, the reaction time, temperature and reagent ratio ( $\text{NaOH}/(\text{NH}_4)_2\text{S}_2\text{O}_8$ ) for NiCo( $\text{OH}$ )<sub>2</sub> growth noticeably influence the electrocatalytic activity of N-NiCoP, and the optimized parameters for NiCo( $\text{OH}$ )<sub>2</sub> preparation are determined (reaction time: 18 h, reaction temperature: 180 °C, and reagent ratio: 0.75). Figs. S4a and S4b show the SEM images of NiCo( $\text{OH}$ )<sub>2</sub>/NCF fabricated under the optimized reaction conditions, and the many micro-sized polyhedron NiCo( $\text{OH}$ )<sub>2</sub> burgeoned from the NCF frame. When the NiCo( $\text{OH}$ )<sub>2</sub>/NCF was treated with different kinds of  $\text{PH}_3$ -Ar/ $\text{N}_2$  plasma at 250 °C (Fig. S5), the HER and OER performances of the NiCoP samples increased greatly, especially with the  $\text{PH}_3/\text{N}_2$  plasma treatment. The reason for explaining the phenomenon may be that the reactive species of N and P generated in  $\text{PH}_3/\text{N}_2$  plasma (Fig. S6) simultaneously reacted with NiCo hydroxides, and the N-doping enhanced the concentration of charge carriers and the electronic conductivity [8].

Fig. 2a and b exhibit the SEM images of polyhedron N-NiCoP/NCF, and the morphology of N-NiCoP shows a similar profile with that of NiCo( $\text{OH}$ )<sub>2</sub>/NCF, as well as the profile of fabricated NiCoP/NCF without using plasma (Figs. S4c and S4d). It should be noted that some cracks occurred on the crystal surface of N-NiCoP, and it may be very useful for exposing larger reaction areas in the electrocatalytic process, thereby causing higher HER and OER activity. Fig. 2c shows the elemental mapping of Co, Ni, P and N on the surface of N-NiCoP/NCF. The homogeneous distribution of these elements on the produced catalyst indicates the N atoms were successfully doped into the NiCoP.

From the TEM (Fig. 2d) and SEM images, it can be seen that different N-NiCoP morphologies were formed on the NCF surface, such as octahedral column- and dodecahedron drum-like. However, they all belong to the cubic crystal system [27], and the irregular structures indicate that the formed NiCo( $\text{OH}$ )<sub>2</sub> crystal profiles serve as a precursor for the cubic shape. Fig. 2e presents the XRD pattern of N-NiCoP/NCF. Compared to the crystal structure of NiCo( $\text{OH}$ )<sub>2</sub>/NCF (Fig. S7), many new crystal phases were formed in the N-NiCoP under the exposure to  $\text{PH}_3/\text{N}_2$  plasmas, such as the planes of (011) at 31.2° for CoP (JCPDS No. 29-0497), (210) at 47.3° for  $\text{Ni}_2\text{P}$  (JCPDS No.16-0116), (311) at 36.8° for  $\text{Co}_2\text{NiP}_4$  (JCPDS No. 02-1074), (211) at 58.5° for  $\text{Ni}_3\text{N}$  (JCPDS No. 10-0280), and (220) at 61.3° for CoN (JCPDS No. 16-0116). These results indicate that most of the NiCo hydroxides have been successfully converted to phosphides.

The composition and chemical states of N-NiCoP were investigated by X-ray photoelectron spectroscopy (XPS). As shown in Fig. 3a and Table S2, the survey spectrum of N-NiCoP revealed the presence of Co, Ni, P, N, O and C elements. Noticeably, the C atoms probably originate from the carbon impurity introduced in the fabrication process of NCF, and the O atoms may be from the unconverted NiCo( $\text{OH}$ )<sub>2</sub> and undecomposed phosphate group ( $\text{PO}_4^{3-}$ ) absorbed on the catalyst surface. Fig. 3b exhibits the high resolution spectrum of the Co 2p peak of N-NiCoP, and the Co 2p spectrum can be deconvoluted into two peaks at 780.5 and 796 eV, which are attributed to the spin-orbit splitting values of the Co 2p<sub>3/2</sub> and Co 2p<sub>1/2</sub> states in the Co-P bond, respectively [33]. The shake-up peaks at 803.7 eV and 785.5 eV are the satellite peaks of Co 2p. Compared to the Co 2p of NiCo( $\text{OH}$ )<sub>2</sub> (bottom line of Fig. 3b), new peaks located at 782.2 and 797.4 eV occurred, and they can attributed to the oxidized Co species in the CoNiP compound, respectively [20,24]. After phosphorization of NiCo( $\text{OH}$ )<sub>2</sub>, the chemical shift of Ni 2p spectrum occurred as shown in Fig. 3c, and the Ni 2p of N-CoNiP peaks along with two satellite peaks at 862.3 and 879.7 eV can be fitted with two peaks at binding energies of 874 (Ni 2p<sub>1/2</sub>) and 856.5 eV (Ni 2p<sub>3/2</sub>) for  $\text{Ni}^{2+}$  in Ni-P, respectively [34]. Note that the peak at 852.3 eV is very near to the metallic nickel (852.6 eV), and it may originate from the NCF substrate [20]. Compared to the XPS spectrum of NiCo( $\text{OH}$ )<sub>2</sub>, N 1 s peak at 399.5 eV occurred in the CoNiP (Fig. 3d). This finding indicates that nitrogen atoms were indeed doped into the CoNi phosphide during the  $\text{N}_2$ - $\text{PH}_3$  plasma treatment. Meanwhile, the deconvoluted N 1 s peaks at 399.0 and 399.8 eV correspond to the Ni-N

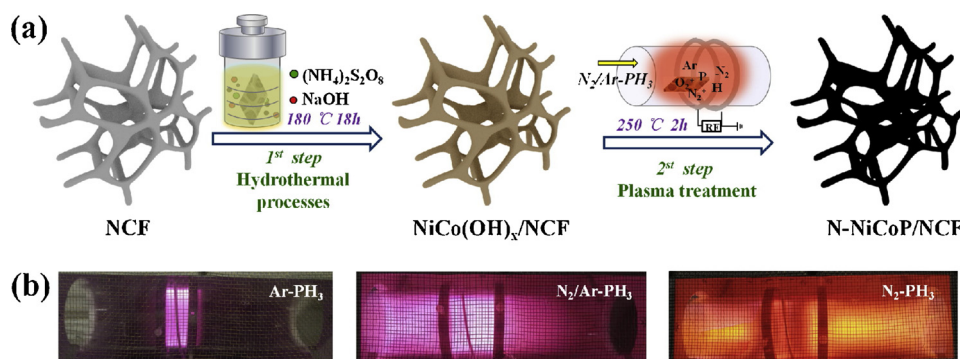
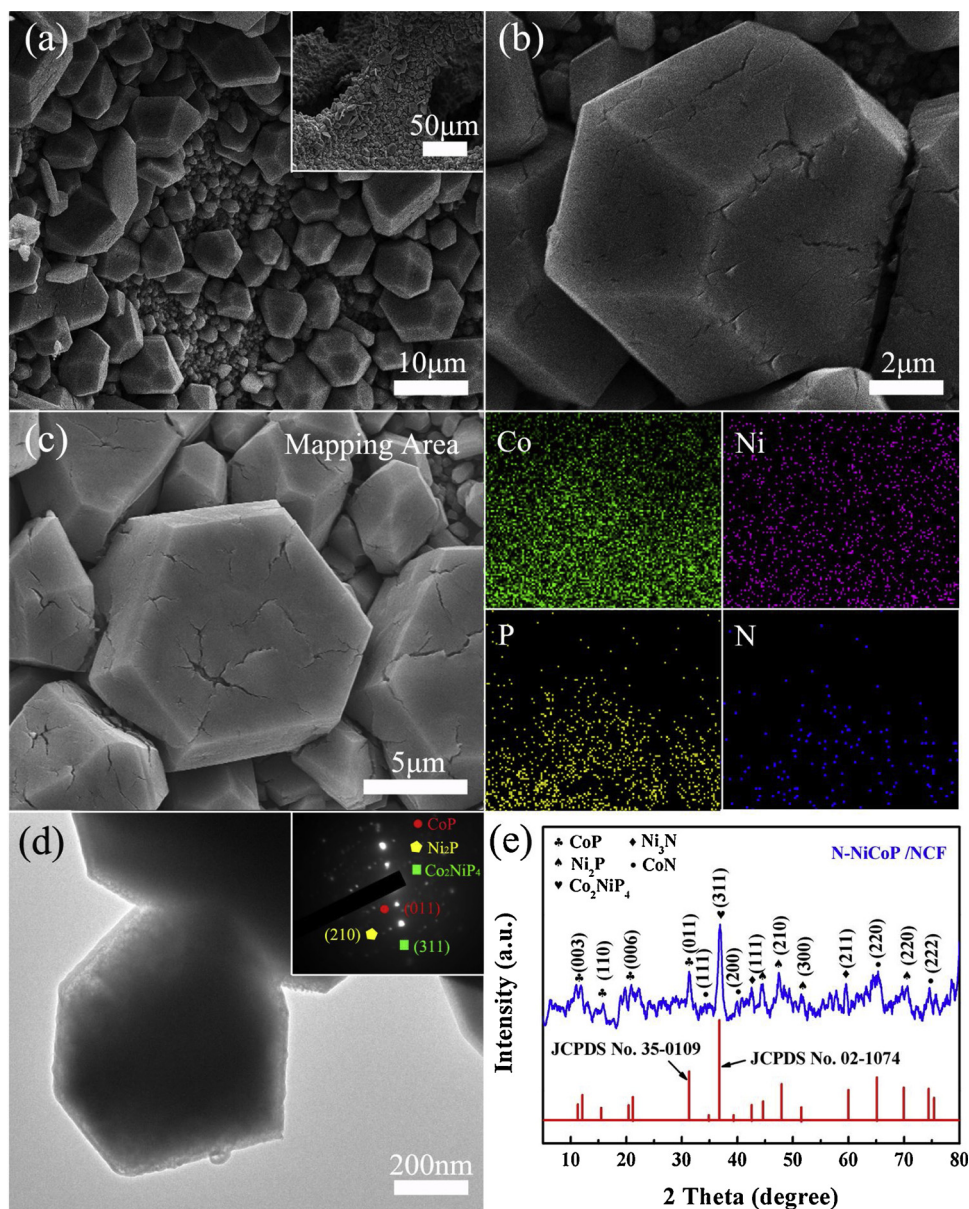


Fig. 1. (a) Schematic of in situ fabrication of N-NiCoP/NCF, and (b) The photographs of plasma discharges in different gas mixtures.





**Fig. 2.** The morphology of N-NiCoP sprouted from the NCF frame. Low (a) and high (b) resolution of SEM images, and the inset in (a) is NCF frame coated with N-NiCoP, (c) SEM mapping area of N-NiCoP and the corresponding elemental distribution of Co, Ni, N, and P respectively, (d) TEM images of N-NiCoP, and (e) XRD pattern of N-NiCoP/NCF samples.

and Co-N bonds, respectively [8,35]. Fig. 3e shows the high-resolution P 2p spectra, which contain two peaks at 128.8 and 133.9 eV, corresponding to P 2p<sub>3/2</sub> state of N-NiCoP and P–O bonds of the PO<sub>4</sub><sup>3−</sup>/P<sub>2</sub>O<sub>5</sub>, respectively [21,36]. Fig. 3f shows the chemical states of O 1s contained in NiCo hydroxide and phosphide. For the two kinds NiCo compound, the peak at 531 eV for O 1s mainly originated from the hydroxide groups [37], while the binding energy of 533 eV corresponds to the absorbed water and NiCoO<sub>x</sub> contained in the oxidized NiCoP [36,38]. Based on the analyses mentioned above, only the shell section of the microsized NiCo(OH)<sub>x</sub> was phosphorized in the plasma reaction process, as opposed to the previously reported phosphorization of the entire nanostructure [36]. Further work is required to improve control of the plasma phosphorization process.

### 3.2. Hydrogen evolution reaction performance

The HER performances of the obtained catalysts were measured in 1 M KOH by means of a standard three-electrode system. Fig. 4a

exhibits the polarization curves of NCF, NiCoP, NiCo(OH)<sub>x</sub>/NCF, N-NiCoP/NCF, and Pt/C. Noticeably, the overpotential of N-NiCoP/NCF for delivering a current density of 10 mA cm<sup>−2</sup> is only 78 mV (Inset of Fig. 4a), which is *much lower* than those of NCF (209 mV), NiCoP (147 mV), NiCo(OH)<sub>x</sub>/NCF (119 mV), and NiCoP/NCF without N doping (105 mV, Fig. S8a). More importantly, the overpotential of N-NiCoP/NCF is also *lower than most of newly reported non-precious electrocatalysts* (Fig. 4b), such as CoP/CFP-H (128.1 mV) [38], Co(S<sub>x</sub>Se<sub>1−x</sub>)<sub>2</sub> (145 mV) [39], CoP (159 mV) [40], 2D-MoS<sub>2</sub>/Co(OH)<sub>2</sub> (128 mV) [41], CoS<sub>2</sub>-TiO<sub>2</sub> (198 mV) [42], NiCu-P (175 mV) [43], NiCoFe-P (231 mV) [44], and Ni<sub>4.3</sub>Co<sub>4.7</sub>S<sub>8</sub> (148 mV) [45], and other catalysts (Table S3).

To study HER kinetics of different catalysts, the Tafel slopes of the catalysts given in Fig. 4a were calculated using the log-scale. As shown in Fig. 4c, the Tafel slope value of N-NiCoP/NCF is only 83.2 mV dec<sup>−1</sup>, which is *far smaller* than those of NiCoP/NCF (138.4 mV dec<sup>−1</sup>, Fig. S8b), NiCo(OH)<sub>x</sub>/NCF (157.1 mV dec<sup>−1</sup>), and NiCoP (178.7 mV dec<sup>−1</sup>), and it follows the Volmer-Heyrovsky mechanism [46]. Meanwhile, the high HER performance of the N-NiCoP/NCF catalyst is also evidenced

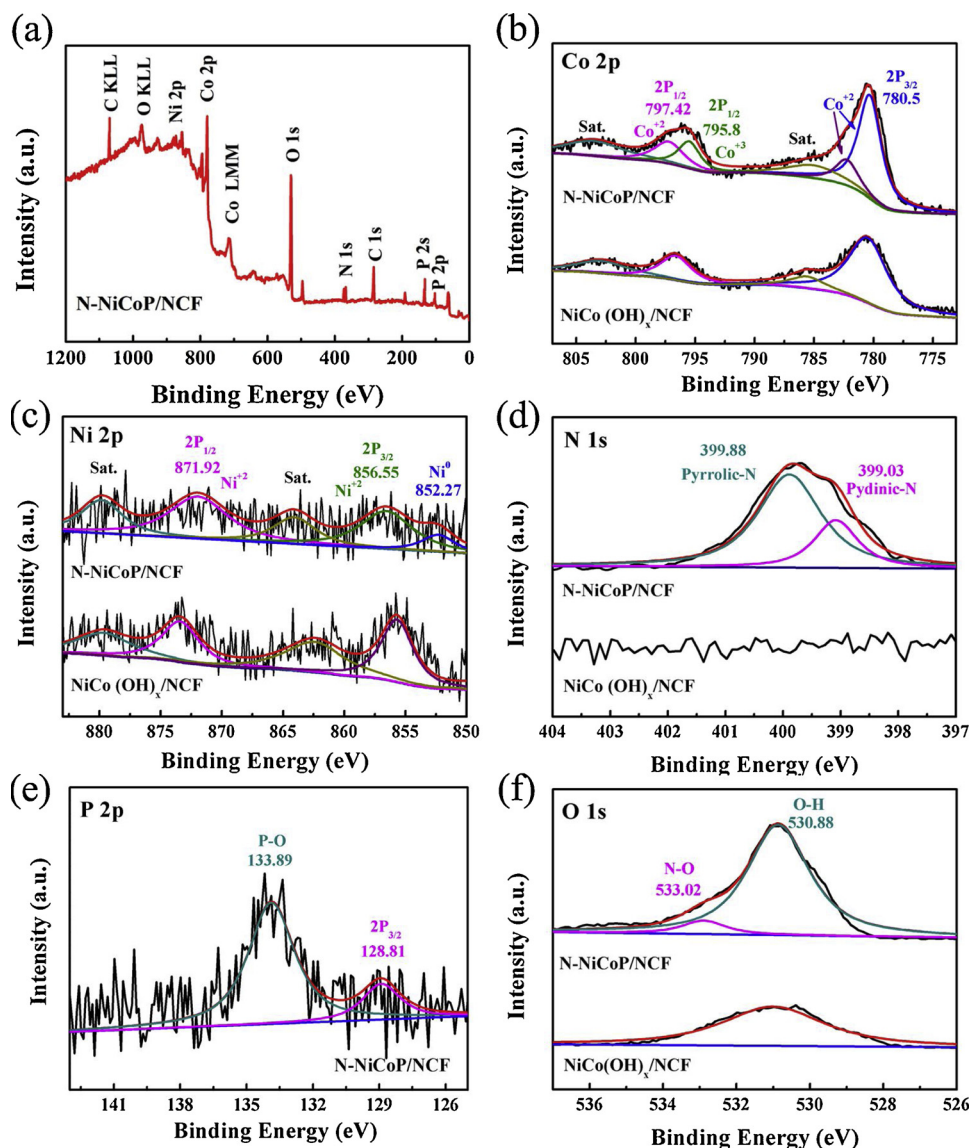


**Fig. 3.** The XPS spectra of NiCo LDH/NCF before and after treatment with  $N_2$ - $PH_3$  plasmas. (a) The chemical states of elements in N-NiCoP/NCF, and peak fitting of (b) Co 2p, (c) Ni 2p, (d) N 1s, and (e) P 2p and (f) O 1s elemental states.

by the *higher*  $H_2$  turn over frequencies (TOFs) than those of NiCoP/NCF and NiCo(OH) $_x$ /NCF (Table S4).

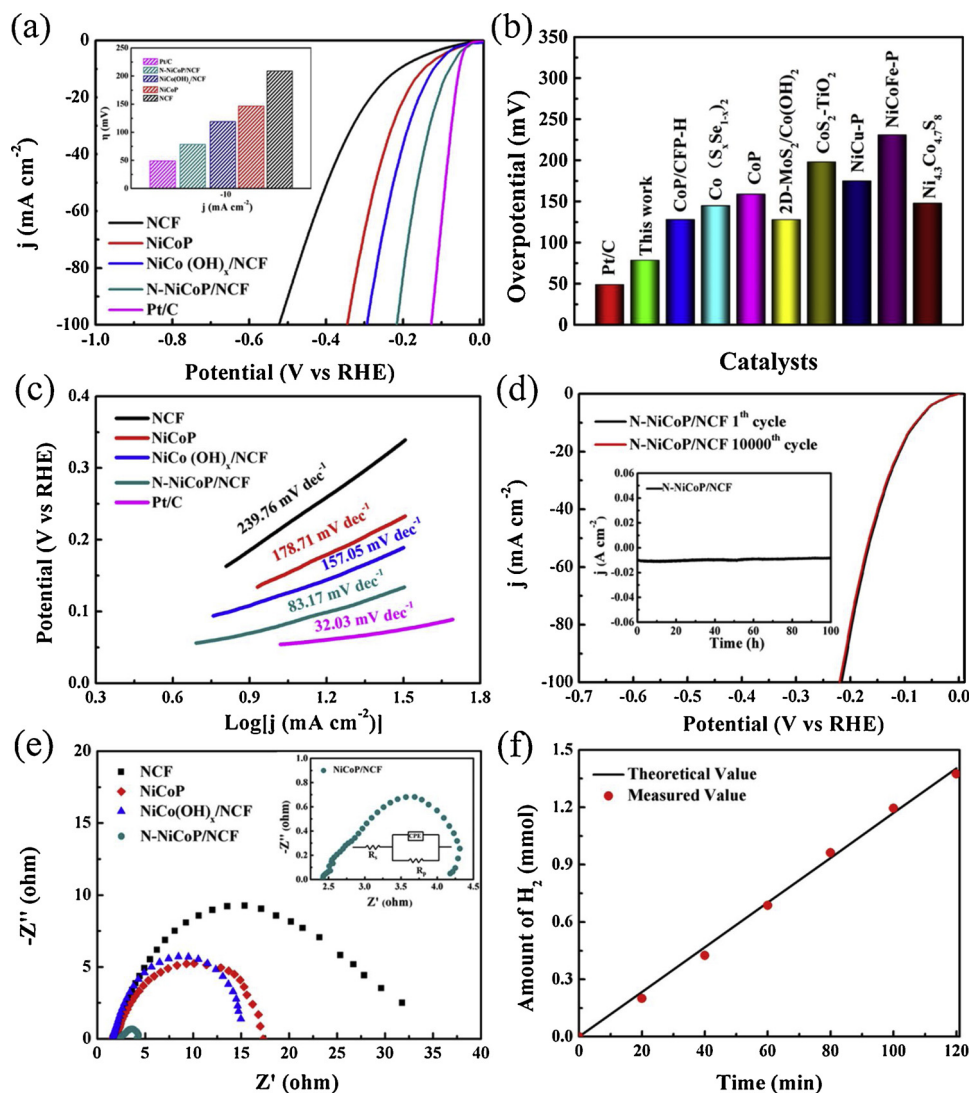
To evaluate the electrocatalytic stability in a strong alkaline medium, a long-term performance test of N-NiCoP/NCF was carried by comparing the LSV curves before and after 10,000 CV cycles. Importantly, the final polarization curve nearly overlaps the initial one (Fig. 4d). Moreover, the *ultra-stable* characteristic of in situ fabricated N-NiCoP/NCF is further confirmed by the I-t curves with a testing time of 100 h, and the initial current density only decreased from 10 to 8.3 mA cm $^{-2}$ . Fig. S9 exhibits the morphology and elemental mapping of N-NiCoP/NCF undergoing 100 h HER test. One can notice that top surfaces of some N-NiCoP/NCF polyhedrons were ablated, and the concentrations of Ni, P and N atoms decreased, which was also proven by the XPS analyses (Fig. S10), XRD (Fig. S11), and Raman (Fig. S12) for the sample measured after 10,000 CV cycles.

Fig. 4e shows the Nyquist plots (EIS) of NCF, NiCoP, NiCo(OH) $_x$ /NCF and N-NiCoP/NCF, and the semicircle diameter corresponds to the interfacial charge transfer resistance ( $R_{ct}$ ). It is clearly revealed that N-NiCoP/NCF exhibits *much smaller* EIS value (1.5  $\Omega$ ) than other electrode materials, indicating a *faster* charge-transfer rate of N-NiCoP/NCF in the alkaline medium for HER process. The amount of  $H_2$  was measured by a

water drainage method, as shown in Fig. 4f, and the N-NiCoP/NCF afforded a *highly stable*  $H_2$  evolution rate of 650  $\mu\text{mol h}^{-1} \text{cm}^{-2}$ , which is *much higher* than those of Fe-Ni $_3$ S $_2$ /NF (500  $\mu\text{mol h}^{-1} \text{cm}^{-2}$ ) [47] and NiFe-P/NF (380  $\mu\text{mol h}^{-1} \text{cm}^{-2}$ ) [48]. In addition, the measured data matched well with the theoretical  $H_2$  amount, indicating an *almost 100% Faradaic efficiency* for HER [49].

### 3.3. Oxygen evolution reaction and overall water splitting

The OER performance of N-NiCoP/NCF was also investigated in 1 M KOH solution using the same three-electrode configuration. Fig. 5a shows the OER polarization curves of NCF, NiCoP, NiCo(OH) $_2$ /NCF, N-NiCoP/NCF, and the commercial RuO $_2$  electrodes in 1.0 M KOH. It can be observed that an overpotential of 225 mV for N-NiCoP/NCF is required to deliver a current density of 10 mA cm $^{-2}$ . Although the value is still higher compared to precious RuO $_2$  (135 mV), it is *far lower* than the NCF (371 mV), NiCoP (336 mV), NiCo(OH) $_2$ /NCF (260 mV), the NiCoP/NCF (250 mV, Fig. S8c), and other reported state-of-the-art non-precious electrocatalysts (Fig. 5b and Table S5). The results mentioned above indicate that N-doping by  $N_2$ - $PH_3$  plasma is a *very effective approach* for fabricating transition metal phosphides for overall water



**Fig. 4.** HER performance of the produced catalysts in 1 M KOH. (a) LSV curves and the overpotentials at a current density of 10 mA cm<sup>-2</sup> (inset), (b) The overpotential comparison between N-NiCoP/NCF and other reported electrocatalysts, (c) Tafel slopes obtained from (a), (d) Polarization curves of N-NiCoP/NCF before and after 10<sup>4</sup> cycles, and the inset is chronoamperometric curve of N-NiCoP/NCF at the current density of 10 mA cm<sup>-2</sup>, (e) Nyquist curves of NCF, NiCoP, NiCo(OH)<sub>2</sub>/NCF and N-NiCoP/NCF, and (f) The H<sub>2</sub> amount of N-NiCoP/NCF generated at a current density of 10 mA cm<sup>-2</sup>.

splitting.

The OER activity of the resulting electrocatalysts was further assessed by the Tafel slope originated from LSV curves of Fig. 5a. As the results shown in Figs. 5c and S8d, the Tafel slopes for NCF, NiCoP, NiCo(OH)<sub>2</sub>/NCF, NiCoP/NCF, N-NiCoP/NCF and RuO<sub>2</sub> are 136, 109, 85, 81, 67 and 46 mV decade<sup>-1</sup>, respectively. The Tafel slope value of N-NiCoP/NCF is close to that of RuO<sub>2</sub>, and is much smaller than that of NiCoP/NCF fabricated without plasma, thus revealing the *robust OER kinetics* of N-NiCoP/NCF in the alkaline medium which is also proven by the larger TOFs in the OER process (Table S6).

The durability of electrocatalysts is very important for continuous OER operation. Fig. 5d presents the polarization curves of N-NiCoP/NCF before and after 10,000 cycles in 1 M KOH, and the LSV curves nearly overlap. It indicates that the in situ prepared N-NiCoP/NCF exhibits *excellent long-term electrocatalytic stability*, which is further confirmed by the low drift of current density (10 to 7.25 mA cm<sup>-2</sup>) in the 100 h continuous OER electrolysis (the inset of Fig. 5d), the stable chemical structures (e.g. XPS: Fig. S10, XRD: Fig. S11, Raman: Fig. S12) for the sample measured after 10,000 CV cycles, especially the unchanged morphology (Fig. S13) after the 100 h OER test. Fig. 5e exhibits the generation amount of O<sub>2</sub> for N-NiCoP/NCF stimulated with a

current density of 10 mA cm<sup>-2</sup> in 1 M KOH, and the generation efficiency is about 400 μmol h<sup>-1</sup> cm<sup>-2</sup>, which is *far higher* than the Ni<sub>x</sub>Co<sub>3-x</sub>S<sub>4</sub>/Ni<sub>3</sub>S<sub>2</sub> (12 μmol h<sup>-1</sup>) [50].

In order to identify the *bifunctional electrocatalytic activity* of N-NiCoP/NCF for overall water splitting, a two-electrode electrolyzer system using the N-NiCoP/NCF as the anode and cathode electrodes in 1 M KOH (N-NiCoP/NCF//N-NiCoP/NCF inset in Fig. 5f) was designed. One can notice that the electrode still exhibits an excellent HER and OER activity in the tested potential region, and the overpotentials for generating a current density of 10 mA cm<sup>-2</sup> in the HER and OER processes are about 79 mV and 1.48 V, respectively. Therefore, the electrolyzer *only needs a very low cell voltage of 1.56 V* to afford a current density of 10 mA cm<sup>-2</sup> for the overall water splitting producing *vigorous gas evolution on both electrodes* (inset in Fig. 5f). Remarkably, the electrocatalytic activity of micro-sized polyhedron N-NiCoP/NCF is clearly *better than most of the state-of-the-art nanomaterials*, such as NiCoP/NF (1.57 V) [20], N-Ni<sub>3</sub>S<sub>2</sub>/VS<sub>2</sub> (1.65 V) [26], NiCo<sub>2</sub>S<sub>4</sub>/CC (1.68 V) [51], f-CoP/CoP<sub>2</sub>/Al<sub>2</sub>O<sub>3</sub> (1.656 V) [25], CoMnCH/NF (1.68 V) [52], and other bifunctional electrocatalysts (Table S7).



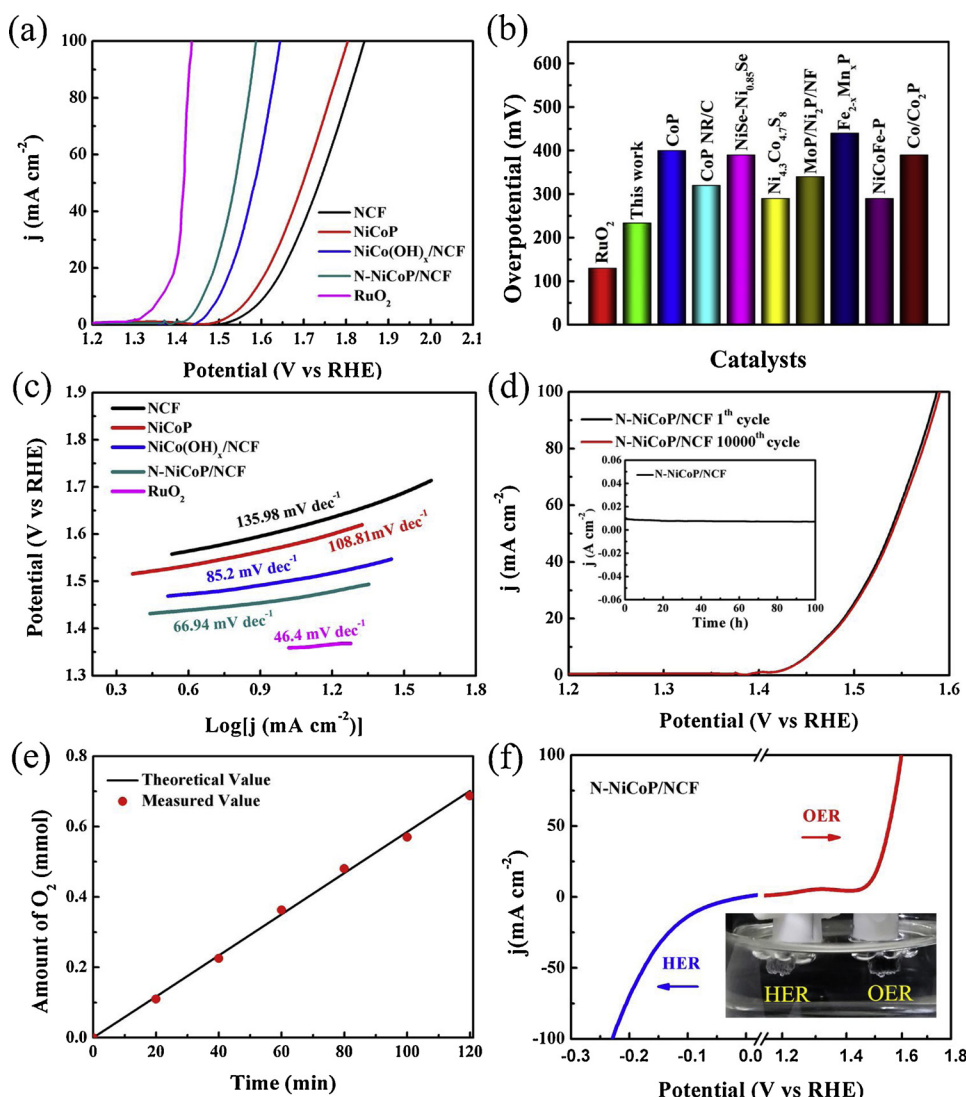


Fig. 5. OER characteristics of the fabricated catalysts in 1 M KOH. (a) LSV curves of different samples, (b) The overpotentials of N-NiCoP/NCF and other state-of-the-art electrocatalysts (e.g. CoP [40], CoP NR/C [53], NiSe-Ni<sub>0.85</sub>Se [17], Ni<sub>4.3</sub>Co<sub>4.7</sub>S<sub>8</sub> [45], MoP/Ni<sub>2</sub>P/NF [46], Fe<sub>2-x</sub>Mn<sub>x</sub>P [54], NiCoFe-P [44], Co/Co<sub>2</sub>P [7]) at a current density of 10 mA cm<sup>-2</sup>, (c) Tafel slopes calculated from (a), (d) Polarization curves of N-NiCoP/NCF before and after 10<sup>4</sup> cycles, and the inset is the long-term stability, (e) The generated amount of O<sub>2</sub> at a current density of 10 mA cm<sup>-2</sup>, and (f) Polarization curves of N-NiCoP/NCF electrodes acting as a bi-functional electrocatalyst for water splitting.

### 3.4. Understanding N-NiCoP with DFT simulations

In order to understand the effect of N doping on the electrocatalytic activity of CoNiP, the density functional theory (DFT) calculations (Vienna *ab initio* Simulation Package, VASP) were performed according to the built crystal models of CoP, Co<sub>0.84</sub>Ni<sub>0.16</sub>P and Co<sub>0.84</sub>Ni<sub>0.16</sub>P<sub>0.84</sub>N<sub>0.16</sub> structures (see Figs. 6a and S14). As shown in Fig. 6b, the calculated density of states (DOS) of CoP, Co<sub>0.84</sub>Ni<sub>0.16</sub>P and Co<sub>0.84</sub>Ni<sub>0.16</sub>P<sub>0.84</sub>N<sub>0.16</sub> electrocatalysts are continuously crossing the Fermi level, indicating their intrinsic metallic properties which is very useful for increasing the electron transfer rate in the electrocatalytic process [8]. Noticeably, using the Ni and N doping one can effectively tune the electronic structure of CoP. Compared to the DOS distribution of CoP shown in Fig. 6b (gray line), the main peak near the Fermi level (-0.2 ~ 0 eV) in Co<sub>0.84</sub>Ni<sub>0.16</sub>P (the magnified red peak in the inset of Fig. 6b) shifts to a lower energy level, which may be mainly caused by the coupling effect of Ni-2p and P-2p covalent pairs [55]. Specifically, the Fermi level of Co<sub>0.84</sub>Ni<sub>0.16</sub>P increases obviously when the N atoms are successfully doped into the catalyst lattice by N<sub>2</sub> plasma (the blue peak in the inset of Fig. 6b). Consequently, the free energy value ( $\Delta G_{H^*}$ ) of Co<sub>0.84</sub>Ni<sub>0.16</sub>P<sub>0.84</sub>N<sub>0.16</sub> (-0.21 eV) is much lower than the catalyst-H\* state of Co<sub>0.84</sub>Ni<sub>0.16</sub>P (Fig. 6c), indicating a low energy barrier for absorbing H\* in the HER process. The whole electron transfer process is sketched in Fig. 6d, and substantially less energy  $\Delta E$  ( $\Delta E < \Delta E^*$ ) is required for N-doped CoNiP to produce H<sub>2</sub> gas in the alkaline media.

### 3.5. OER and HER enhancement mechanism

Based on the experimental and theory results, the in situ fabricated N-NiCoP/NCF polyhedron exhibits highly-active and ultra-stable electrocatalytic performances for both HER and OER in an alkaline medium. The reasons for the superior bi-functional activity and stability of N-NiCoP/NCF are as follows:

- The NiCo alloy foam acting as a substrate of N-NiCoP exhibits the high electrocatalytic activity for HER and OER (Figs. 4 and 5). Meanwhile, the obtained electrocatalyst features the core/shell (NiCo(OH)<sub>x</sub>/NiCoP) structure, and the multiple crystal phases (e.g., Ni<sub>2</sub>P, CoP, Co<sub>2</sub>NiP<sub>4</sub>, CoN, Ni<sub>3</sub>N) of N-doped NiCoP form rich heterointerfaces, which are very useful for increasing reaction kinetics of the HER and OER processes;
- The N<sub>2</sub>/PH<sub>3</sub> plasma formed a higher density of P and N on the catalyst surface than can be achieved by a similar thermal process without plasmas (Fig. S15 and Table S1). Moreover, the N-doping changes the Fermi level (Figs. 6b and S14), causing a higher electrical conductivity, which can increase the electron transfer rate and improve the bi-functional electrocatalytic performances [11];
- The DFT results indicate that the N-NiCoP has a lower absorption free energy of H ( $\Delta G(H^*)$ ) and the H\*-state more easily occurs on the catalyst surface, enhancing the whole catalytic activity for

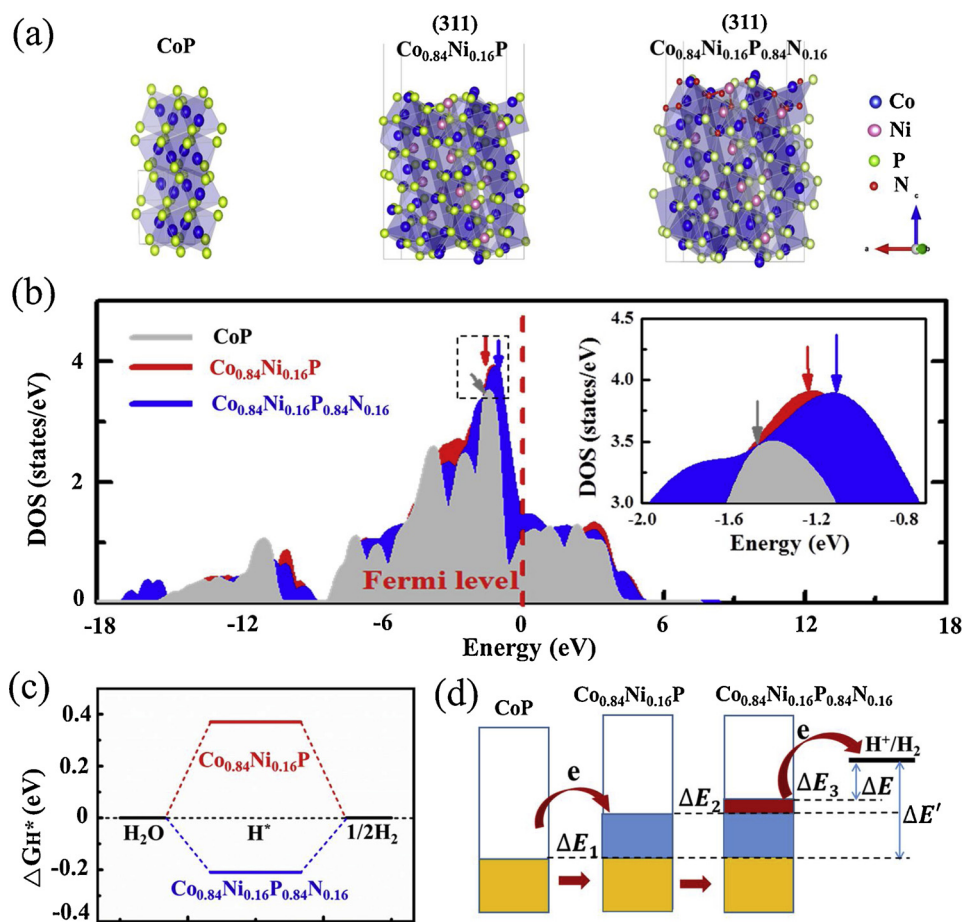


Fig. 6. (a) The crystal structures of CoP, Co<sub>0.84</sub>Ni<sub>0.16</sub>P, and Co<sub>0.84</sub>Ni<sub>0.16</sub>P<sub>0.84</sub>N<sub>0.16</sub> constructed based on the XRD and XPS results, (b) The calculated density of states for CoP, Co<sub>0.84</sub>Ni<sub>0.16</sub>P, and Co<sub>0.84</sub>Ni<sub>0.16</sub>P<sub>0.84</sub>N<sub>0.16</sub>, (c) HER free energy before and after N doping, and (d) The schematic energy level of Ni and N atoms doped into 2H-CoP to form Co<sub>0.84</sub>Ni<sub>0.16</sub>P and Co<sub>0.84</sub>Ni<sub>0.16</sub>P<sub>0.84</sub>N<sub>0.16</sub>, and the charge transfer in the HER process.

- HER.
- (iv) The reaction process of N<sub>2</sub>-PH<sub>3</sub> plasmas increases the catalytic area of N-NiCoP/NCF, indicated by the calculated  $C_{dl}$  (18.16 mF cm<sup>-2</sup>) which is much higher than the NiCo(OH)<sub>x</sub>/NCF (12.28 mF cm<sup>-2</sup>) and NCF (5.97 mF cm<sup>-2</sup>), as shown in Fig. S16. Meanwhile, the synergistic effect of core-shell heterostructured NiCo(OH)<sub>x</sub>/N-NiCoP may play an important role in the achieved high electrocatalytic activity for overall water splitting [46];
- (v) As the fabricated micro-sized N-NiCoP polyhedron sprout in situ directly from the NCF frame, the resulting strong coupling between the electrocatalyst and the NCF, is favourable to substantially improve electrocatalytic performance. In addition, the anti-corrosive properties of micro-sized N-NiCoP in the electrolysis medium are far better than those of the previously reported nanosized phosphides [20,36]. As a result, the obtained N-NiCoP/NCF are produced in a sustainable way (which minimizes materials use) and exhibits ultrastable electrocatalytic activity, especially for the OER process.

#### 4. Conclusion

In summary, the N-doped core-shell of NiCo(OH)<sub>x</sub>/NiCoP polyhedron was in situ fabricated on the NCF frame, and the obtained electrocatalyst exhibits an excellent bi-functional activity for overall water splitting in an alkaline medium. For HER and OER, the overpotentials of N-NiCoP/NCF for delivering a current density of 10 mA cm<sup>-2</sup> are only 78 and 225 mV, respectively. Meanwhile, the H<sub>2</sub> and O<sub>2</sub> amounts generated by the N-NiCoP/NCF catalyst at a current density of 10 mA cm<sup>-2</sup> are about 0.65 and 0.4 mmol h<sup>-1</sup>, respectively. The high electrocatalytic activity and efficiency of N-NiCoP/NCF outperformed most of the recently reported non-noble electrocatalysts. More

importantly, the in situ fabricated N-NiCoP/NCF exhibits ultrastable electrocatalytic performances for HER and OER after the 100 h test, especially for the OER process where no morphology changes of the N-NiCoP/NCF catalyst were observed. This work opens new avenues for in situ fabrication of transition metal based electrocatalysts for highly efficient and stable overall water splitting and other applications in energy and catalysis fields.

#### Acknowledgements

This work is financially supported by National Natural Science Foundation of China under Grant Nos. 11665005, 51862001, 51672249, 11804301, 11505032, Zhejiang Natural Science Foundations of China under Grant No. LY16A050002, Natural Science Foundation of Jiangxi Province under Grant Nos. 20171BAB211012, 20171ACB21049, 20161BAB211026, Science and Technology Project of Jiangxi Provincial Department of Education under Grant Nos. GJJ170823, GJJ170843, and K. O. appreciates the Australian Research Council for partial support.

#### Appendix A. Supplementary data

Supplementary material related to this article can be found, in the online version, at doi:<https://doi.org/10.1016/j.apcatb.2019.04.089>.

#### References

- [1] S. Chu, A. Majumdar, Opportunities and challenges for a sustainable energy future, *Nature* 488 (2012) 294–303, <https://doi.org/10.1038/nature11475>.
- [2] S. Cu, Y. Cui, N. Liu, The path towards sustainable energy, *Nat. Mater.* 16 (2017) 16–22, <https://doi.org/10.1038/nmat4834>.
- [3] T.A. Pham, Y. Ping, G. Galli, Modelling heterogeneous interfaces for solar water



- splitting, *Nat. Mater.* 16 (2017) 401–408, <https://doi.org/10.1038/nmat4803>.
- [4] B. Zhang, X. Zheng, O. Voznyy, R. Comin, M. Bajdich, M.G. Melchor, L. Han, J. Xu, M. Liu, L. Zheng, F.P.G. Arquer, C.T. Dinh, F. Fan, M. Yuan, E. Yassitepe, N. Chen, T. Regier, P. Liu, Y. Li, P. Luna, A. Janmohamed, H.L. Xin, H. Yang, A. Vojvodic, E.H. Sargent, Homogeneously dispersed multimetal oxygen-evolving catalysts, *Science* 352 (2016) 333–337, <https://doi.org/10.1126/science.aaf1525>.
  - [5] M.D. Symes, L. Cronin, Decoupling hydrogen and oxygen evolution during electrolytic water splitting using an electron-coupled-proton buffer, *Nat. Chem.* 5 (2013) 403–409, <https://doi.org/10.1038/nchem.1621>.
  - [6] X. Zheng, B. Zhang, P. Luna, Y. Liang, R. Comin, O. Voznyy, L. Han, F.P.G. Arquer, M. Liu, C.T. Dinh, T. Regier, J.J. Dynes, S. He, H.L. Xin, H. Peng, D. Prendergast, X. Du, E.H. Sargent, Theory-driven design of high-valence metal sites for water oxidation confirmed using in situ Soft x-ray absorption, *Nat. Chem.* 10 (2018) 149–154, <https://doi.org/10.1038/nchem.2886>.
  - [7] J. Masa, S. Barwe, C. Andronescu, I. Sinev, A. Ruff, K. Jayaramulu, K. Elumeeva, B. Konkena, B.R. Cuenya, W. Schuhmann, Low overpotential water splitting using cobalt-cobalt phosphide nanoparticles supported on nickel foam, *ACS Energy Lett.* 1 (2016) 1192–1198, <https://doi.org/10.1021/acsenenergylett.6b00532>.
  - [8] P. Chen, T. Zhou, M. Zhang, Y. Tong, C. Zhong, N. Zhang, L. Zhang, C. Wu, Y. Xie, 3D nitrogen-anion-decorated nickel sulfides for highly efficient overall water splitting, *Adv. Mater.* 29 (2017) 1701584, <https://doi.org/10.1002/adma.201701584>.
  - [9] J.S. Luo, J.H. Im, M.T. Mayer, M. Schreier, M.K. Nazeeruddin, N.G. Park, S.D. Tilley, H.J. Fan, M. Grätzel, Water photolysis at 12.3% efficiency via perovskite photo-voltaics and Earth-abundant catalysts, *Science* 345 (2014) 1593–1596, <https://doi.org/10.1126/science.1258307>.
  - [10] I. Roger, M.A. Shipman, M.D. Symes, Earth-abundant catalysts for electrochemical and photoelectrochemical water splitting, *Int. Rev. Chem. Eng.* 1 (2017) 0003, <https://doi.org/10.1038/s41570-016-0003>.
  - [11] Z.W. Seh, J. Kibsgaard, C.F. Dickens, I. Chorkendorff, J.K. Nørskov, T.F. Jaramillo, Combining theory and experiment in electrocatalysis: insights into materials design, *Science* 355 (2017) 4998–5009, <https://doi.org/10.1126/science.aad4998>.
  - [12] D. Voiry, H. Yamaguchi, J. Li, R. Silva, D.C.B. Alves, T. Fujita, M. Chen, T. Asefa, V.B. Shenoy, G. Eda, M. Chhowalla, Enhanced catalytic activity in strained chemically exfoliated WS<sub>2</sub> nanosheets for hydrogen evolution, *Nat. Mater.* 12 (2013) 850–855, <https://doi.org/10.1038/nmat3700>.
  - [13] H. Li, S. Chen, Y. Zhang, Q. Zhang, X. Jia, Q. Zhang, L. Gu, X. Sun, L. Song, X. Wang, Systematic design of superaerophobic nanotube-array electrode comprised of transition-metal sulfides for overall water splitting, *Nat. Commun.* 9 (2018) 2452, <https://doi.org/10.1038/s41467-018-04888-0>.
  - [14] Y. Liu, J. Wu, K.P. Hackenberg, J. Zhang, Y.M. Wang, Y. Yang, K. Keyshar, J. Gu, T. Ogitsu, R. Vajtai, J. Lou, P.M. Ajayan, B.C. Wood, B.I. Yakobson, Self-optimizing, highly surface-active layered metal dichalcogenide catalysts for hydrogen evolution, *Nat. Energy* 2 (2017) 17127, <https://doi.org/10.1038/nenergy.2017.127>.
  - [15] J.W. Su, Y. Yang, G.L. Xia, J.T. Chen, P. Jiang, Q.W. Chen, Ruthenium-cobalt nanoalloys encapsulated in nitrogen-doped graphene as active electrocatalysts for producing hydrogen in alkaline media, *Nat. Commun.* 8 (2017) 14969, <https://doi.org/10.1038/ncomms14969>.
  - [16] Z. Wang, Y. Inoue, T. Hisatomi, R. Ishikawa, Q. Wang, T. Takata, S. Chen, N. Shibata, Y. Ikuhara, K. Domen, Overall water splitting by Ta<sub>3</sub>N<sub>5</sub> nanorod single crystals grown on the edges of KTaO<sub>3</sub> particles, *Nat. Catal.* 1 (2018) 756–763, <https://doi.org/10.1038/s41929-018-0134-1>.
  - [17] Y. Chen, Z. Ren, H. Fu, X. Zhang, G. Tian, H. Fu, NiSe-Ni<sub>0.85</sub>Se heterostructure nanoflake arrays on carbon paper as efficient electrocatalysts for overall water splitting, *Small* 14 (2018) 1800763, <https://doi.org/10.1002/sml.201800763>.
  - [18] Y. Zheng, P. Wu, M. Gao, X. Zhang, F. Gao, H. Ju, R. Wu, Q. Gao, R. You, W. Huang, S. Liu, S. Hu, J. Zhu, Z. Li, S. Yu, Doping-induced structural phase transition in cobalt diselenide enables enhanced hydrogen evolution catalysis, *Nat. Commun.* 9 (2018) 2533, <https://doi.org/10.1038/s41467-018-04954-7>.
  - [19] Y. Yu, G. Nam, Q. He, X. Wu, K. Zhang, Z. Yang, J. Chen, Q. Ma, M. Zhao, Z. Liu, F. Ran, X. Wang, H. Li, X. Huang, B. Li, Q. Xiong, Q. Zhang, Z. Liu, L. Gu, Y. Du, W. Huang, H. Zhang, High phase-purity 1T'-MoS<sub>2</sub> and 1T'-MoSe<sub>2</sub>-layered crystals, *Nat. Chem.* 10 (2018) 638–643, <https://doi.org/10.1038/s41557-018-0035-6>.
  - [20] J. Li, G. Wei, Y. Zhu, Y. Xi, X. Pan, Y. Ji, I.V. Zatonovskiy, W. Han, Hierarchical NiCoP nanocone arrays supported on Ni foam as an efficient and stable bifunctional electrocatalyst for overall water splitting, *J. Mater. Chem. A Mater. Energy Sustain.* 5 (2017) 14828–14837, <https://doi.org/10.1039/C7TA03947F>.
  - [21] C. Guan, W. Xiao, H. Wu, X. Liu, W. Zhang, H. Zhang, J. Ding, Y.P. Feng, S.J. Pennycook, J. Wang, Hollow Mo-doped CoP nanoarrays for efficient overall water splitting, *Nano Energy* 48 (2018) 73–80, <https://doi.org/10.1016/j.nanoen.2018.03.034>.
  - [22] J.X. Feng, S.Y. Tong, Y.X. Tong, G.R. Li, Pt-like hydrogen evolution electrocatalysis on PANI/CoP hybrid nanowires by weakening the shackles of hydrogen ions on the surfaces of catalysts, *J. Am. Chem. Soc.* 140 (2018) 5118–5126, <https://doi.org/10.1021/jacs.7b12968>.
  - [23] H.F. Liang, A.N. Gandhi, D.H. Anjum, X.B. Wang, U. Schwingenschlögl, H.S.N. Alshareef, Plasma-assisted synthesis of NiCoP for efficient overall water splitting, *Nano Lett.* 16 (2016) 7718–7725, <https://doi.org/10.1021/acs.nanolett.6b03803>.
  - [24] E. Hu, Y. Feng, J. Nai, D. Zhao, Y. Hu, X.W. Lou, Construction of hierarchical Ni-Co-P hollow nanobricks with oriented nanosheets for efficient overall water splitting, *Energy Environ. Sci.* 11 (2018) 872–880, <https://doi.org/10.1039/C8EE00076J>.
  - [25] W. Li, S. Zhang, Q. Fan, F. Zhang, S. Xu, Hierarchically scaffolded CoP/CoP<sub>2</sub> nanoparticles: controllable synthesis and their application as a well-matched bifunctional electrocatalyst for overall water splitting, *Nanoscale* 9 (2017) 5677–5685, <https://doi.org/10.1039/C7NR01017F>.
  - [26] X.W. Zhong, J. Tang, J.W. Wang, M. Shao, J.W. Chai, S.P. Wang, M. Yang, Y. Yang, N. Wang, S.J. Wang, B.M. Xu, H. Pan, 3D heterostructured pure and N-Doped Ni<sub>3</sub>S<sub>2</sub>/VS<sub>2</sub> nanosheets for high efficient overall water splitting, *Electrochim. Acta* 269 (2018) 55–61, <https://doi.org/10.1016/j.electacta.2018.02.131>.
  - [27] T. Odedairo, X.C. Yan, X.D. Yao, K. Ostrikov, Z.H. Zhu, Hexagonal sphericon hematite with high performance for water oxidation, *Adv. Mater.* 29 (2017) 1703792, <https://doi.org/10.1002/adma.201703792>.
  - [28] S. Qu, W. Chen, J. Yu, G. Chen, R. Zhang, S. Chu, J. Huang, X. Wang, C. Li, K. Ostrikov, Cross-linked trimetallic nanopetals for electrocatalytic water splitting, *J. Power Sources* 390 (2018) 224–233, <https://doi.org/10.1016/j.jpowsour.2018.04.061>.
  - [29] X. Chen, P. Li, Z. Jin, Y. Meng, H. Yuan, D. Xiao, Tri-metallic phytate in situ electrodeposited on 3D Ni foam as a highly efficient electrocatalyst for enhanced overall water splitting, *J. Mater. Chem. A* 5 (2017) 18786–18792, <https://doi.org/10.1039/C7TA05386J>.
  - [30] F. Lyu, Y. Bai, Z. Li, W. Xu, Q. Wang, J. Mao, L. Wang, X. Zhang, Y. Yin, Self-templated fabrication of CoO-MoO<sub>2</sub> nanocages for enhanced oxygen evolution, *Adv. Funct. Mater.* 27 (2017) 1702324, <https://doi.org/10.1002/adfm.201702324>.
  - [31] S.J. Chu, W. Chen, G.L. Chen, J. Huang, R. Zhang, C. Song, X. Wang, C. Li, K. Ostrikov, Holey Ni-Cu phosphide nanosheets as a highly efficient and stable electrocatalyst for hydrogen evolution, *Appl. Catal. B- Environ.* 243 (2019) 537–545, <https://doi.org/10.1016/j.apcatb.2018.10.063>.
  - [32] M.C. Payne, M.P. Teter, D.C. Allan, T.D. Arias, J.D. Joannopoulos, Iterative minimization techniques for ab initio total-energy calculations: molecular dynamics and conjugate gradients, *Rev. Mod. Phys.* 64 (1992) 1045–1097, <https://doi.org/10.1103/RevModPhys.64.1045>.
  - [33] Q. Fu, T. Wu, G. Fu, T. Gao, J. Han, T. Yao, Y. Zhang, W. Zhong, X. Wang, B. Song, Skutterudite-type ternary Co<sub>1-x</sub>Ni<sub>x</sub>P<sub>3</sub> nanonoodle array electrocatalysts for enhanced hydrogen and oxygen evolution, *ACS Energy Lett.* 3 (2018) 1744–1752, <https://doi.org/10.1021/acsenenergylett.8b00908>.
  - [34] Q. Zhang, D. Yan, Z. Nie, X. Qiu, S. Wang, J. Yuan, D. Su, G. Wang, Z. Wu, Iron-doped NiCoP porous nanosheet arrays as a highly efficient electrocatalyst for oxygen evolution reaction, *ACS Appl. Energy Mater.* 1 (2018) 571–579, <https://doi.org/10.1021/acsaem.7b00143>.
  - [35] Y. Wang, C. Xie, Z. Zhang, D. Liu, R. Chen, S. Wang, In situ exfoliated, N-Doped, and edge-rich ultrathin layered double hydroxides nanosheets for oxygen evolution reaction, *Adv. Funct. Mater.* 28 (2018) 1703363, <https://doi.org/10.1002/adfm.201703363>.
  - [36] C. Du, L. Yang, F.L. Yang, G.Z. Cheng, W. Luo, Nest-like NiCoP for highly efficient overall water splitting, *ACS Catal.* 7 (2017) 4131–4137, <https://doi.org/10.1021/acscatal.7b00662>.
  - [37] P. Guo, J. Wu, X.B. Li, J. Luo, W.M. Lau, H. Liu, X.L. Sun, L.M. Liu, A highly stable bifunctional catalyst based on 3D Co(OH)<sub>2</sub>@NCNTs@NF towards overall water-splitting, *Nano Energy* 47 (2018) 96–104, <https://doi.org/10.1016/j.nanoen.2018.02.032>.
  - [38] S.H. Yu, D.H.C. Chua, Toward high-performance and low-cost hydrogen evolution reaction electrocatalysts: nanostructuring cobalt phosphide (CoP) particles on carbon Fiber paper, *ACS Appl. Mater. Interfaces* 10 (2018) 14777–14785, <https://doi.org/10.1021/acsaami.8b02755>.
  - [39] L. Fang, W. Li, Y. Guan, Y. Feng, H. Zhang, S. Wang, Y. Wang, Tuning unique peapod-like Co(S<sub>2</sub>Se<sub>1-x</sub>)<sub>2</sub> nanoparticles for efficient overall water splitting, *Adv. Funct. Mater.* 27 (2017) 1701008, <https://doi.org/10.1002/adfm.201701008>.
  - [40] M. Liu, J. Li, Cobalt phosphide hollow polyhedron as efficient bifunctional electrocatalysts for the evolution reaction of hydrogen and oxygen, *ACS Appl. Mater. Interfaces* 8 (2016) 2158–2165, <https://doi.org/10.1021/acsaami.5b10727>.
  - [41] Z. Zhu, H. Yin, C. He, M. Mamun, P. Liu, L. Jiang, Y. Zhao, Y. Wang, H.G. Yang, Z. Tang, D. Wang, X.M. Chen, H. Zhao, Ultrathin transition metal dichalcogenide/3d metal hydroxide hybridized nanosheets to enhance hydrogen evolution activity, *Adv. Mater.* 30 (2018) 1801171, <https://doi.org/10.1002/adma.201801171>.
  - [42] P. Ganesan, A. Sivanantham, S. Shanmugam, CoS<sub>2</sub>-TiO<sub>2</sub> hybrid nanostructures: efficient and durable bifunctional electrocatalysts for alkaline electrolyte membrane water electrolyzers, *J. Mater. Chem. A* 6 (2018) 1075–1085, <https://doi.org/10.1039/C7TA09096J>.
  - [43] M. Asnavandi, B.H.R. Suryanto, W. Yang, X. Bo, C. Zhao, Dynamic hydrogen bubble templated NiCu phosphide electrodes for pH-insensitive hydrogen evolution reactions, *ACS Sustain. Chem. Eng.* 6 (2018) 2866–2871, <https://doi.org/10.1021/acssuschemeng.7b02492>.
  - [44] M.A.Z.G. Sial, H. Lin, X. Wang, Microporous 2D NiCoFe phosphate nanosheets supported on Ni foam for efficient overall water splitting in alkaline media, *Nanoscale* 10 (2018) 12975–12980, <https://doi.org/10.1039/C8NR03350A>.
  - [45] Y. Tang, H. Yang, J. Sun, M. Xia, W. Guo, L. Yu, J. Yan, J. Zheng, L. Chang, F. Gao, Phase-pure pentlandite Ni<sub>4.3</sub>Co<sub>4.7</sub>S<sub>9</sub> binary sulfide as an efficient bifunctional electrocatalyst for oxygen evolution and hydrogen evolution, *Nanoscale* 10 (2018) 10459–10466, <https://doi.org/10.1039/C8NR02402B>.
  - [46] C. Du, M. Shang, J. Mao, W. Song, Hierarchical MoP/Ni<sub>2</sub>P heterostructures on nickel foam for efficient water splitting, *J. Mater. Chem. A* 5 (2017) 15940–15949, <https://doi.org/10.1039/C7TA03669H>.
  - [47] G. Zhang, Y.S. Feng, W.T. Lu, D. He, C.Y. Wang, Y.K. Li, X.Y. Wang, F.F. Cao, Enhanced catalysis of electrochemical overall water splitting in alkaline media by Fe doping in Ni<sub>3</sub>S<sub>2</sub> nanosheet arrays, *ACS Catal.* 8 (2018) 5431–5441, <https://doi.org/10.1021/acscatal.8b00413>.
  - [48] J.H. Xing, H. Li, M.M.C. Cheng, S.M. Geyerb, K.Y. Simon Ng, Electro-synthesis of 3D porous hierarchical Ni-Fe phosphate film/Ni foam as a high-efficiency bifunctional electrocatalyst for overall water splitting, *J. Mater. Chem. A* 4 (2016) 13866–13873, <https://doi.org/10.1039/C6TA05952J>.
  - [49] Y. Hu, F. Li, Y. Long, H. Yang, L. Gao, X. Long, H. Hu, N. Xu, J. Jin, J. Ma, Ultrafine

- CoPS nanoparticles encapsulated in N, P, and S tri-doped porous carbon as an efficient bifunctional water splitting electrocatalyst in both acid and alkaline solutions, *J. Mater. Chem. A* 6 (2018) 10433–10440, <https://doi.org/10.1039/C8TA01310A>.
- [50] Y. Wu, Y. Liu, G.D. Li, X. Zou, X. Lian, D. Wang, L. Sun, T. Asefa, X. Zou, Efficient electrocatalysis of overall water splitting by ultrasmall  $\text{Ni}_x\text{Co}_{3-x}\text{S}_4$  coupled  $\text{Ni}_3\text{S}_2$  nanosheet arrays, *Nano Energy* 35 (2017) 161–170, <https://doi.org/10.1016/j.nanoen.2017.03.024>.
- [51] H. Chen, J. Jiang, L. Zhang, D. Xia, Y. Zhao, D. Guo, T. Qi, H. Wan, In situ growth of  $\text{NiCo}_2\text{S}_4$  nanotube arrays on Ni foam for supercapacitors: maximizing utilization efficiency at high mass loading to achieve ultrahigh areal pseudocapacitance, *J. Power Sources* 254 (2014) 249–257, <https://doi.org/10.1016/j.jpowsour.2013.12.092>.
- [52] T. Tang, W.J. Jiang, S. Niu, N. Liu, H. Luo, Y.Y. Chen, S.F. Jin, F. Gao, L.J. Wan, J.S. Hu, Electronic and morphological dual modulation of cobalt carbonate hydroxides by Mn doping toward highly efficient and stable bifunctional electrocatalysts for overall water splitting, *J. Am. Chem. Soc.* 139 (2017) 8320–8328, <https://doi.org/10.1021/jacs.7b03507>.
- [53] J. Chang, Y. Xiao, M. Xiao, J. Ge, C. Liu, W. Xing, Surface oxidized cobalt-phosphide nanorods As an advanced oxygen evolution catalyst in alkaline solution, *ACS Catal.* 5 (2015) 6874–6878, <https://doi.org/10.1021/acscatal.5b02076>.
- [54] D. Li, H. Baydoun, B. Kulikowski, S.L. Brock, Boosting the catalytic performance of Iron phosphide nanorods for the oxygen evolution reaction by incorporation of manganese, *Chem. Mater.* 29 (2017) 3048–3054, <https://doi.org/10.1021/acs.chemmater.7b00055>.
- [55] D. Wang, X. Wang, Y. Lu, C. Song, J. Pan, C. Li, M. Sui, W. Zhao, F.Q. Huang, Atom-scale dispersed palladium in a conductive  $\text{Pd}_{0.1}\text{TaS}_2$  lattice with a unique electronic structure for efficient hydrogen evolution, *J. Mater. Chem. A* 5 (2017) 22618–22624, <https://doi.org/10.1039/C7TA06447K>.